Journal of Catalysis 334 (2016) 1–13

Contents lists available at ScienceDirect

Journal of Catalysis

journal homepage: www.elsevier.com/locate/jcat

Novel manganese oxide confined interweaved titania nanotubes for the low-temperature Selective Catalytic Reduction (SCR) of NO_x by NH_3

Dimitrios K. Pappas [a], Thirupathi Boningari [a], Punit Boolchand [b], Panagiotis G. Smirniotis [a],*

[a] Chemical Engineering Program, School of Energy, Environmental, Biological and Medical Engineering, University of Cincinnati, Cincinnati, OH 45221-0012, United States
[b] Department of Electrical and Computer Science Engineering, University of Cincinnati, Cincinnati, OH 45221-0012, United States

ARTICLE INFO

Article history:
Received 3 June 2015
Revised 29 September 2015
Accepted 8 November 2015
Available online 17 December 2015

Keywords:
Low-temperature NH_3-SCR
Nitrogen oxides (NO_x)
Manganese oxide (MnO_x)
Titania nanotubes

ABSTRACT

A series of manganese confined titania nanotubes (Mn/TNT) prepared by alkaline hydrothermal synthesis technique and were investigated for the Selective Catalytic Reduction (SCR) of NO_x with NH_3 in the presence of excess (10 vol.%) oxygen. Remarkably, the surface texture and tubular morphology of Mn/TNT-H catalyst greatly promote the NO_x conversions in the temperature regime of 100–300 °C. The existence of abundant surface Mn^{4+} species apparently contributes to the remarkable low-temperature SCR activity, and additionally the increased surface area, high dispersion and numerous Lewis acid sites distribution contribute to broaden temperature window over Mn/TNT-H catalyst with 0.25 Mn/Ti atomic ratio. The impregnation of MnO_x over TNT-SA catalyst occurs bare minimum because of the low specific surface area and low pore volume, and this leads to poor deNO_x activity. The Mn^{4+}/Mn^{3+} fraction deduced by XPS found to be considerably high for the Mn(0.25)/TNT-H catalyst ($Mn^{4+}/Mn^{3+} = 2.15$) while in other catalysts the fraction is typically in the range of 0.36–1.34. Raman scattering reveals a redshift of 13 cm^{-1} from 640 cm^{-1} (TiO_2-Hombikat) to 627 cm^{-1} in Mn/TNTs-H sample, which indicates the formation of a new phase or structural difference. In comparison with the Mn supported on TiO_2 (Hombikat) nanoparticles, the Mn species on the developed tubular Mn/TNT-H were less pronounced to coagulate under the reaction temperatures. It is interesting to note that the relative atomic ratios of Mn^{4+}/Ti and Mn^{4+}/Mn^{3+} as well as the existence of surface Mn^{4+} species in the titania nanotube appear to be directly correlated with the deNO_x performance of the catalysts.

1. Introduction

The Selective Catalytic Reduction (SCR) of NO_x using ammonia (NH_3) as the reducing agent is a well-established and efficient process for the abatement of nitrogen oxide (NO_x) emissions. The prevailing commercial catalytic formulation consists of V_2O_5 supported on TiO_2 (anatase), frequently promoted by WO_3 or MoO_3, having an operating temperature window from 300 to 400 °C [1,2]. The high temperature required for the operation of the catalyst influences its performance due to the presence of SO_2 and soot. The development of catalytic formulations active in low temperature region will help to resolve issues caused by SO_2 oxidation and poisoning, and moreover will assist the widespread utilization of SCR units by the automotive industry in order to achieve the abatement of NO_x emitted by automobile sources. Selective catalytic reduction of NO_x by urea (urea/SCR) is the most efficient technology for the aftertreatment of NO_x from diesel engine exhaust to meet stringent emission regulations, including EURO VI and SULEV [3]. An SCR catalyst is required to be active, particularly in the low temperature regimes, since the normal exhaust gas temperature from a diesel engine ranging from 100 to 250 °C for light duty to 200–350 °C for heavy duty diesel engines is significantly lower than that from a gasoline engine, and the exhaust temperature from an advanced diesel engine for high fuel efficiency is foreseeable to become even lower [4,5].

It has been well reported in the literature that the manganese oxide-based catalysts supported on TiO_2 nanoparticles exhibit promising deNO_x potential in the low temperature region [1,6–9]. Manganese oxide-based catalysts supported on various TiO_2 (anatase, rutile and mixed phases) exhibit higher catalytic activities. In our earlier studies, we have reported high surface area (309 m^2/g) anatase TiO_2 (Hombikat) as a superior support compared to other types of commercially available TiO_2 [7–10].

---

* Corresponding author. Tel.: +1 (513) 556 1474; fax: +1 (513) 556 3473.
E-mail address: panagiotis.smirniotis@uc.edu (P.G. Smirniotis).

http://dx.doi.org/10.1016/j.jcat.2015.11.013
0021-9517/© 2015 Elsevier Inc. All rights reserved.

Subsequently, novel titania nanotubes prepared by alkaline hydrothermal treatment can provide a high surface area and a unique nanotubular structure which can be beneficial for the higher dispersion of the active species and improve the deNO$_x$ potential of manganese oxide-based formulations.

Recently, titania nanotubes have been attracted significant attention for their utilization in catalysis [11–13]. Metal oxide-based catalysts supported on titania nanotubes utilized for the low-temperature SCR of NO$_x$ by NH$_3$ is a research in primary stages. Some researchers reported copper oxide [14,15], ceria [16–20], and vanadia [21] supported on titania nanotubes for the SCR of NO by NH$_3$. However, most of the reported nanotubes have shown activity in the medium and high temperatures regimes. To date, no manganese confined titania nanotubes have been synthesized and investigated for the remarkable low-temperature (100–300 °C) SCR of NO$_x$ with NH$_3$ in the presence of excess (10 vol.%) oxygen.

In the present work, various TiO$_2$ nanoparticles with numerous crystallographic phases, particle size and surface area were used to prepare titania nanotubes via the alkaline hydrothermal treatment method. The resulting titania nanotubes possess different morphological features such as specific surface area, length and diameter due to the different characteristics of TiO$_2$ nanoparticles used for their synthesis. The main objective of our present work is not only to screen titania nanotube supports and optimize the manganese content for the SCR of NO$_x$ reaction, but more significantly, it seeks to elucidate the structural-performance correlation of the catalyst. These factors allow a broad variation of the manganese loading together with an excellent anchoring of the manganese species onto the various titania nanotubes.

The catalytic activity of the manganese confined titania nanotubes (Mn/TNTs) was investigated for the low temperature SCR of NO$_x$ by NH$_3$ at a GHSV of 50,000 h^{-1} in the presence of excess oxygen. The Mn/TNT-H catalyst exhibits remarkable deNO$_x$ potential at temperatures as low as 100 °C and a wide temperature window up to 300 °C. Our X-ray photoelectron spectroscopy studies illustrate that the relative atomic percentage value of Mn^{4+}/Mn^{3+} characterized by deconvoluted XPS spectra was considerably high for the Mn(0.25)/TNT-H catalyst (Mn^{4+}/Mn^{3+} = 2.15) whereas, surface Mn^{3+} species are in equivalence with MnO$_2$ phase in other catalysts (Mn^{4+}/Mn^{3+} = 0.36–1.34). For the layered tubular structures, existence of abundant surface Mn^{4+} species contributes to the remarkable low-temperature SCR activity, additionally increased surface area, and high dispersion and rich Lewis acid sites distribution contribute to broad temperature window over Mn(0.25)/TNT-H catalyst. This contribution demonstrates the use of spectroscopic, physicochemical techniques to study the effect of various supports in the nanotubular structure, reduction profiles and surface atomic compositions for the remarkable selective catalytic reduction at low-temperatures.

2. Experimental

2.1. Synthesis of TiO$_2$ nanoparticles from titanium oxysulfate

A required amount of the precursor was dissolved in deionized water and then stirring and heating were applied. The resulting solution was washed with deionized water in order to remove sulfates and the precipitant was dried in over at 80 °C, finally grinded in mortar and then sieved using a mesh with 300 μm opening.

2.2. Synthesis of titania nanotubes

Various TiO$_2$ nanoparticles (Hombikat, Ishihara, Sigma–Aldrich, P25 Degussa, Kemira, and TiO$_2$ prepared using titanium oxysulfate) with numerous crystallographic phases, particle size and surface area were used as precursors for the titania nanotubes synthesis. Hereafter, these titania nanotubes were denoted as TNT-H, TNT-I, TNT-SA, TNT-P25, TNT-K, and TNT-TOS, respectively.

The synthesis of the titania nanotubes was achieved by dissolving 2 g of TiO$_2$ in 70 mL of 10 M NaOH solution and hydrothermally treated at 130 °C for 24 h in a Teflon-lined stainless steel autoclave. After the thermal treatment, the content of the autoclaves was filtered and washed initially with deionized water followed by 2 L of 0.2 M HCl aqueous solution until the pH reached approximately 1–2 and finally washed again with deionized water until the pH was resorted to neutral. The resulting nanotubes were dried at the low temperature of 80 °C for 18 h in order to avoid agglomeration of the structure. Finally, the material was grinded in mortar and sieved in a mesh with 300 μm openings. The resulting titania nanotubes are denoted as TNT-X where X indicates the TiO$_2$ precursor used for the preparation as can be observed in Table 1 along with the corresponding specific surface area (m^2/g) of the materials.

2.3. Synthesis of Mn(0.25)/TNT-X (X = H, SA, I, P25, K, and TOS) and Mn(x)/TNT-H (x = Mn/Ti atomic ratio) nanotube catalysts

2.3.1. Screening of nanotube supports and optimization of manganese content for the SCR of NO$_x$

Initially, we have prepared a series of titania nanotubes by alkaline hydrothermal synthesis method using various titania precursors such as TiO$_2$ (Ishihara), TiO$_2$ (Kemira), TiO$_2$ P25 (Degussa), TiO$_2$ (Sigma–Aldrich), TiO$_2$ (Hombikat), and TiO$_2$ synthesized from titanium oxysulfate (TOS). Consequently, manganese oxide confined titania nanotube catalysts were prepared by adopting the incipient wetness technique. In a typical synthesis procedure, manganese nitrate hydrate (MnN$_2$O$_6$·xH$_2$O 99.99% trace metal basis from Sigma–Aldrich) was an active metal precursor. For the first family of catalysts, we have screened by aiming at the preeminent nanotube support for the SCR of NO$_x$ reaction by altering the titania precursor. For this purpose, the manganese loadings were selected as 15 wt.% and the support titania nanotubes (TNT-H, TNT-I, TNT-SA, TNT-P25, TNT-K, and TNT-TOS) varied as described in the earlier section. For the second family of catalysts, we have synthesized a series of manganese oxide confined titania nanotube (Mn/TNT-H) catalysts with different manganese to titania atomic ratio (Mn/Ti = 0.15, 0.20, 0.25, 0.30, and 0.35) by adopting the incipient wetness technique.

For this purpose, the required amount of precursor was added to a 100 mL beaker containing 1.0 g of support in 50 mL deionized water. The excess water was then slowly evaporated on a water bath with continuous stirring at 70 °C. For comparison purposes, we also prepared conventional Mn/TiO$_2$ (Hombikat) catalyst. The resulting materials were oven dried at 120 °C for 12 h, and were ground and sieved (80–120 mesh) to obtain homogeneous powder. Prior to the reaction studies, the powder was calcined in a tubular oven at 400 °C for 2 h under continuous air flow (150 mL min^{-1}). The metal components of the catalysts are denoted as atomic ratios. All the ratios of the catalysts in this study are Mn/Ti = 0.15, 0.20, 0.25, 0.30, and 0.35. For example, Mn(0.25)/TNT-H indicates that the atomic ratio of manganese/titania is 0.25 and the titania nanotube support was synthesized by alkaline hydrothermal treatment of TiO$_2$ Hombikat.

2.4. Materials characterization

The specific surface area (m^2/g), pore volume (cm^3/g), average pore diameter (nm), adsorption desorption isotherms and pore size distribution of the synthesized titania nanotubes and the resulting manganese oxide based catalytic formulations were obtained from N$_2$ adsorption isotherms at liquid nitrogen temperature (77 K)

Table 1
Specific surface area, pore volume measurements and isotherm type, hysteresis loop type of titania nanotubes.

TiO_2[a]	SSA (m^2/g)	TiO_2 nanotubes[b]	SSA (m^2/g)	Pore volume (cm^3/g)	Pore diameter (nm)	Isotherm type	Hysteresis loop type
TiO_2 (Hombikat)	309	TNT-H	421	0.75	7.1	V	H3
TiO_2 (Ishihara PT-101)	25	TNT-I	236	0.71	11.9	V	H1
TiO_2 (Degussa P25)	57	TNT-P25	418	1.56	15.0	V	H1
TiO_2 (Kemira)	54	TNT-K	315	1.13	14.4	V	H1
TiO_2 (Sigma Aldrich)	51	TNT-SA	82	0.29	14.2	V	H1
TiO_2 (TOS)	274	TNT-TOS	334	0.40	4.8	VI	H3

[a] Pristine titania precursors used for the synthesis of titania nanotubes.
[b] Titania nanotubes prepared by adopting hydrothermal synthesis technique.

using a surface area and porosimetry analyzer (Micromeritics Tristar 3000) analyzer. Specific surface area, pore volume measurements, isotherm type, and hysteresis loop type of titania nanotubes are presented in Table 1.

XRD patterns of the materials were obtained using a Phillips Xpert diffractometer occupied with nickel-filtered Cu Kα radiation source. The intensity data were collected over a 2θ range of 10–80° with a step size of 0.025° and a step time of 0.25 s. The crystalline phases of the materials were determined by comparing the XRD patterns to the reference data from International Center for Diffraction Data (ICDD) files.

XPS was used to analyze the atomic surface concentration on selected manganese oxide confined titania nanotube formulations. The X-ray Photoelectron Spectroscopy (XPS) experiments were carried out on a Pyris-VG thermo scientific X-ray photoelectron spectrometer system equipped with a monochromatic Al Kα (1486.7 eV) as a radiation source at 300 W under UHV (6.7×10^{-8} Pa). Sample charging during the measurement was compensated by an electron flood gun. The electron takeoff angle was 45° with respect to the sample surface. The spectra were recorded in the fixed analyzer transmission mode with pass energies of 89.45 and 35.75 eV for recording survey and high resolution spectra, respectively. The powdered catalysts were mounted onto the sample holder and evacuated overnight at room temperature at a pressure on the order of 10^{-7} torr. Binding energies (BE) were measured for C 1*s*, O 1*s*, Mn 2*p* and Ti 2*p*. Sample charging effects were eliminated by correcting the observed spectra with the C 1*s* binding energy (BE) value of 284.6 eV. An estimated error of ±0.2 eV can be considered for all the measurements. The overlapped Mn 2*p* peaks were deconvoluted into several sub-bands by searching for the optimal combination of Gaussian bands with the correlation coefficients (r^2) above 0.99. The Mn 2*p* peak was deconvoluted using the Gaussian function.

Hydrogen-Temperature Programmed Reduction (H_2-TPR) of the manganese oxide confined titania nanotube catalysts was carried out in a catalyst characterization system (Micromeritics, model AutoChem II 2910). The hydrogen consumption of the materials in the temperature range from 75 to 700 °C is obtained by integrating the thermal conductivity detector (TCD) signal.

Ammonia-Temperature Programmed Desorption (NH_3-TPD) data were collected using the same automated catalyst characterization system (Micromeritics Autochem II 2910). The samples were saturated with anhydrous NH_3 and then flushed with helium in order to remove weakly bound (physisorbed) NH_3. Finally the ammonia desorption patterns were obtained by gradually increasing the temperature from 75 to 700 °C.

The Raman spectra of the synthesized titania nanotubes and the corresponding catalytic formulations were obtained using a triple stage Raman spectrometer (T64000 Horiba Jobin Yvon), equipped with a microscope (Olympus BX-41) and optical multichannel detector (CCD array) using He–He laser. The spectral resolution of the analysis was 0.631 cm^{-1} and ranges from 10 to 1000 cm^{-1}. The overlapped Raman peaks were deconvoluted into sub-bands by searching for the optimal combination of Gaussian bands with the correlation coefficients (r^2) from 0.95 to 0.99 (PeakFit, Version 4.0.6, AISN Software Inc.) with 95% confidence limits.

In order to determine the morphological features of the nanotubes and manganese oxide confined titania nanotube formulations, high resolution transmission electron microscopic (HR-TEM) images were taken with a FEI Tecnai F30 transmission electron microscope (TEM) operated at 200 kV.

2.5. Apparatus and catalytic experiments

The potential catalytic performance of the prepared manganese oxide confined titania nanotube catalysts in the low-temperature SCR of NO_x by NH_3 with excess (10 vol.%) oxygen was tested at atmospheric pressure in a continuous flow fixed bed quartz reactor. The predetermined amount of the synthesized catalyst was placed in the reactor in between two glass wool plugs. All the gas flows were measured and calibrated using a digital flow meter (Humonics Hewlett Packard Optiflow 520). The reaction gas mixture consisted of 900 ppm NO, 100 ppm NO_2, 1000 ppm NH_3 and 10 vol.% O_2 and ultra-high purified helium (UHP helium 99.999%) as balance. The premixed gases oxygen (20% in He, Wright Brothers), ammonia (3.99% in He, Wright Brothers) and nitrogen oxides (1.8% NO + 0.2% NO_2 in He, Wright Brothers) were used as received. The NO and NO_2 concentrations were constantly monitored by a chemiluminescence NO/NO_x detector (Eco Physics CLD 70S). To avoid errors caused by the oxidation of ammonia in the converter of the NO/NO_x analyzer, an ammonia trap containing phosphoric acid solution was installed before the sample inlet to the chemiluminescence detector. The reactor was heated externally via a tubular furnace regulated by a temperature controller. The fresh catalysts were evaluated starting at 100–300 °C with 20 °C increments (temperature ramp up). The reactants and products were analyzed using a chemiluminescence detector (Eco Physics CLD 70S) and *on-line* Quadrapole mass spectrometer (MKS PPT-RGA). Reactant and product contents in the reactor effluent were recorded only after steady state was achieved at each temperature step. The N2 selectivity and NO conversions were calculated as in our previous papers [1,7–10].

3. Results and discussion

3.1. Selective Catalytic Reduction (SCR) of NO_x with NH_3 at low-temperatures

Initially, we evaluated the potential catalytic performance of first family of catalysts (Mn/TNT-SA, Mn/TNT-P25, Mn/TNT-K, Mn/TNT-I, Mn/TNT-TOS, and Mn/TNT-H with Mn/Ti atomic ratio = 0.25) in the temperature range of 100–300 °C to screen for the best support and to ensure the influence of various titania precursors on NO_x conversion (Fig. 1).

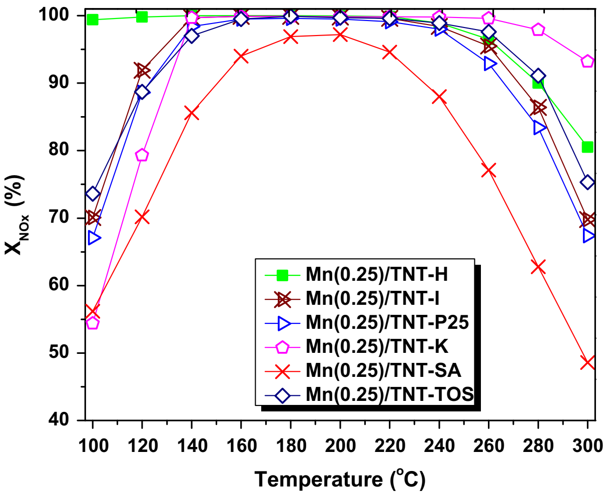

Fig. 1. Catalytic evaluation of the Mn(0.25)/TNT-X (X = Hombikat, Ishihara, P25 Degussa, Kemira, Sigma–Aldrich, and Titania oxysulfate) family of catalyst for the SCR of NO_x by NH_3, in the presence of 900 ppm NO, 100 ppm NO_2, 1000 ppm NH_3, 10 vol.% O_2 with He balance under a GHSV of 50,000 h^{-1} in the temperature range from 100 to 300 °C.

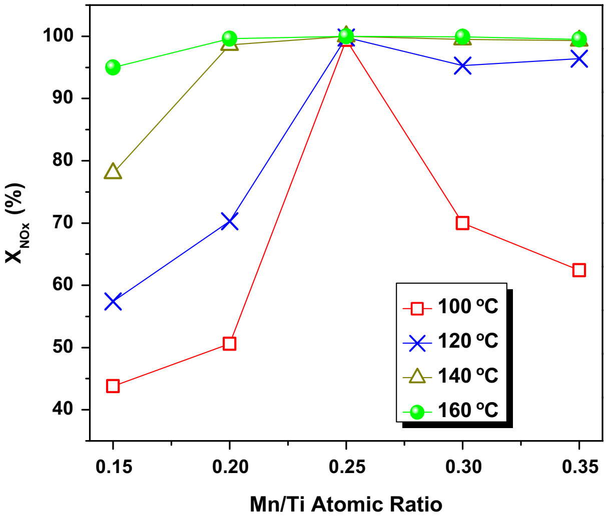

Fig. 2. Effect of Mn/Ti ratio on the performance of Mn(x)/TNT-H family of catalysts for the SCR of NO_x by NH_3, in the presence of 900 ppm NO, 100 ppm NO_2, 1000 ppm NH_3, 10 vol.% O_2 with He balance under a GHSV of 50,000 h^{-1} at 100, 120, 140 and 160 °C.

From our results, one can observe that the manganese loading into the numerous titania nanotubes could indeed influence the SCR activity at low-temperatures. In the present investigation, the textural properties of various titania nanotube supports (TNT-H, TNT-I, TNT-SA, TNT-P25, TNT-K and TNT-TOS) and their influence on surface MnO_x sites for NH_3-SCR activities were studied (Fig. 1). Interestingly, manganese oxide confined titania nanotubes showed a remarkable low-temperature deNO_x performance and broad temperature window in the presence of excess (10 vol.%) oxygen. In particular, Mn(0.25)/TNT-H sample demonstrated impressive NO_x conversions in the temperature range of 100–300 °C in comparison with other catalysts (Fig. 1), which may be attributed to the higher surface area (421 m^2/g) of the TNT-H support, and high dispersion of active components. Among all the catalysts tested, Mn/TNT-SA showed poor deNO_x performance due to the low surface area (82 m^2/g) and porevolume.

To get insights into the optimal content of manganese oxide supported on the TNT-H, the catalytic performance results for the SCR of NO_x with ammonia over manganese confined titania nanotubes (Mn/TNT-H) catalysts with different manganese to titania atomic ratio (Mn/Ti = 0.15, 0.20, 0.25, 0.30, and 0.30) are tested at GHSV 50,000 h^{-1} in the presence of 10 vol.% of oxygen (Fig. 2). The Mn/Ti atomic ratio has a strong influence on the NO_x conversion, since manganese loading with the Mn/Ti ratio = 0.25 catalyst exhibits a maximum conversion of 100% in the temperature range of 100–160 °C (Fig. 2). This would indicate that an optimal dispersion of Mn species over the support surface is attained with this amount of manganese in the Mn/TNT-H catalyst. The Mn/TNT-H catalyst with Mn/Ti = 0.15 does not accomplish high NO_x conversions at 100 °C, 120 °C, and 140 °C. As the Mn/Ti atomic ratio increases up to 0.25 in the catalyst, the NO_x conversion increased monotonically and then dropped for higher loadings (Mn/Ti = 0.30, 0.35) of manganese. As can be noted from Fig. 2, high conversion of NO_x (100%) achieved over the Mn(0.25)/TNT-H catalyst at all the temperatures tested.

As indicated by the catalytic evaluations (Figs. 1 and 2) and the relative turnover frequency calculations (Table 2), Mn(0.25)/TNT-H sample exhibits superior activity compared to the rest of the samples.

The poor activity of the catalysts with low Mn/Ti ratio can be attributed to the lack of active catalytic sites due to the low loading of manganese oxide. Further increment in the Mn loading led to the coagulation of the manganese particles in the titania nanotube.

The higher activity of the Mn(0.25)/TNT-H nanotubes can be attributed to the higher accessibility of the reactants to active sites compared to the other catalysts. Remarkably, the surface texture and tubular morphology of titanium oxide greatly promoted the NO_x conversions and activity temperature window (Figs. 1 and 2), which can be ascribed to the preferentially located manganese species in the tubular framework.

We also investigated the deNO_x performance of conventional Mn-loaded titania nanoparticles (Mn/TiO_2) and Mn-loaded titania nanotubes (Mn-TNT-H) samples for the structure related comparison (Fig. 3). As we can see from Fig. 3, structural changes (spherical nanoparticles of titania transformed to open-ended with multiwall nanotubes) in the catalyst also promoted the catalytic activities.

3.2. Water vapor tolerance, durability and hysteresis effect in catalytic activity

Initially, we have evaluated the potential catalytic performance of our Mn(0.25)/TNT-H catalyst for 6 h in the absence of H_2O vapors to ensure the time on stream stability. The premixed gases oxygen (20% in He, Wright Brothers), ammonia (4% in He, Wright Brothers), and nitrogen oxides (2.0% in He, Wright Brothers) were used as received. ISCO series D pump controller was used to feed the 10 vol.% concentration of water vapor. The typical reaction conditions were as follows: gas hourly space velocity (GHSV) = 50,000 h^{-1}; feed: NO = 900 ppm, NO_2 = 100 ppm, NH_3 = 1000 ppm, O_2 = 10 vol.%, He carrier gas. Afterward, 10 vol.% of H_2O vapors added continuously to the reaction feed for 72 h to investigate the water vapor tolerance and durability of our catalyst (Fig. 4). As can be seen from Fig. 4, our Mn(0.25)/TNT-H catalyst demonstrated imposing catalytic activity by exhibiting steady conversions (Fig. 4) at 140 °C. A total of 10 vol.% H_2O vapors were used for the hydrothermal stability test. The introduction of manganese into the titania nanotubes with 0.25 Mn/Ti atomic ratio produced very stable and durable catalyst that did not deactivate for the tested period. The NO_x conversions of the catalyst remained same after 72 h on stream. These results clearly suggest that the Mn (0.25)/TNT-H illustrates a satisfactory extent of stability and

Table 2
Specific surface area, pore volume, pore diameter, reduction temperature, active metal dispersion, reaction rates, and turnover frequency at 100 °C.

Catalyst	SSA (m^2/g)	Pore volume (cm^3/g)	Pore diameter (nm)	Dispersion (%)[a]	Reaction rate ($\mu mol\ g^{-1}\ s^{-1}$)[b]	TOF (s^{-1})[c]	*T* (°C)[d]			H_2 consumption ($\mu m\ g^{-1}$)
							T_1	T_2	T_3	
Mn(0.25)/TNT-H	221	0.47	8.5	71.3	5.81E−02	0.29	309	388	–	2212.2
Mn(0.25)/TNT-I	161	0.46	11.3	64.6	4.09E−02	0.23	306	386	547	2447.6
Mn(0.25)/TNT-P25	197	0.76	15.4	65.5	3.91E−02	0.21	332	406	542	2988.9
Mn(0.25)/TNT-K	196	0.80	16.4	59.7	3.18E−02	0.19	342	430	594	2706.4
Mn(0.25)/TNT-SA	55	0.23	16.7	57.4	3.28E−02	0.20	340	411	–	2518.2
Mn(0.25)/TNT-TOS	161	0.22	5.5	60.5	4.29E−02	0.26	329	410	–	2306.3
Mn(0.15)/TNT-H	238	0.55	9.1	–	–	–	344	415	–	1270.9
Mn(0.20)/TNT-H	252	0.58	9.1	–	–	–	336	413	–	1812.0
Mn(0.30)/TNT-H	200	0.47	9.3	–	–	–	357	449	–	2682.9
Mn(0.35)/TNT-H	192	0.45	9.3	–	–	–	340	405	–	3035.9
Mn(0.25)/TiO_2	166	0.37	9.2	–	–	–	308	404	482	2471.1

[a] Fraction or percentage of manganese atoms at the surface.
[b] Reaction rate at 100 °C.
[c] Turnover frequency (TOF) or Site time yield (STY): number of NO_x molecules converted per manganese atom site per second.
[d] From temperature programmed reduction.

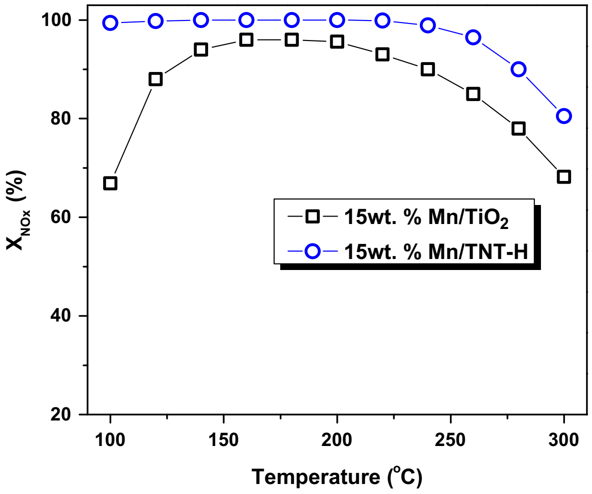

Fig. 3. Catalytic activity comparison of Mn(0.25)/TiO_2 and Mn(0.25)/TNT-H samples; Reaction conditions: NO = 900 ppm, NO_2 = 100 ppm, NH_3 = 1000 ppm, O_2 = 10 vol.%, balance He and GHSV = 50,000 h^{-1}.

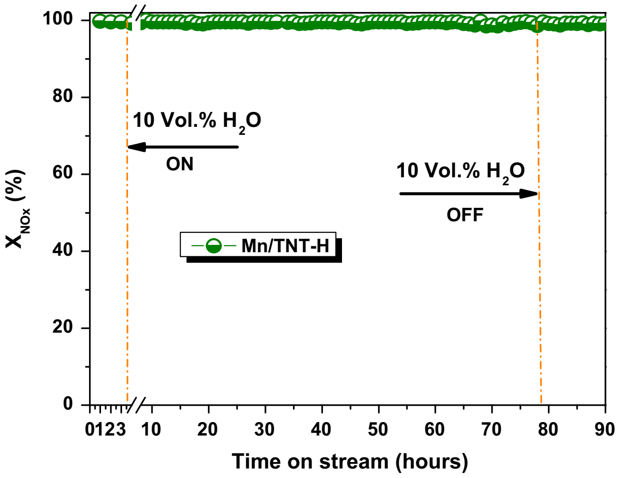

Fig. 4. Influence of inlet water concentrations (10 vol.%) on NO_x conversion in the SCR reaction over Mn(0.25)/TNT-H catalyst at 140 °C; feed: NO = 900 ppm, NO_2 = 100 ppm NH_3/NO_x (ANR) = 1.0, O_2 = 10 vol.%, He carrier gas, GHSV. 50,000 h^{-1}.

durability properties. The system is successful because of its high activity and resistance to steam poisoning. The addition of H_2O (10 vol.%) in the feed gas does not seem to create an eternal alteration to the surface active components, most probably due to the existence of highly active and redox potential pairs of Mn^{4+} and Mn^{3+} preferentially located in the tubular framework, permitting an efficient active catalyst.

Further, we have investigated the Mn(0.25)/TNT-H catalyst for durability and hysteresis effect in catalytic activity (Fig. 5). Initially, reaction temperature was ramped up from 100 °C to 300 °C and then ramped down to 100 °C with 20 °C interval. As one can see from Fig. 5, Mn(0.25)/TNT-H catalyst demonstrated high deNO$_x$ performance and no hysteresis effect in the catalytic activity.

3.3. Specific surface area and pore size distribution

The specific surface area (m^2/g) of all the synthesized titania nanotubes obtained by N_2 physisorption at liquid nitrogen temperature is depicted in Table 1. These results illustrate that the alkaline hydrothermal treatment of TiO_2 results in enhanced specific surface area compared to the primitive TiO_2 nanoparticles [12,22,23]. From the results, it is clear that the TiO_2 Hombikat possesses the high specific surface area (SSA = 309 m^2/g) among the

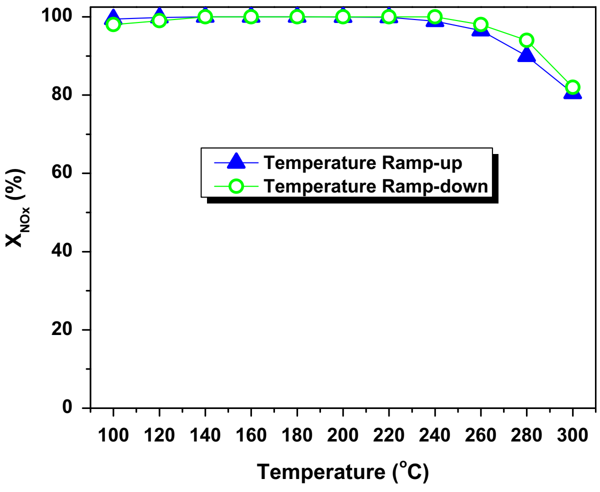

Fig. 5. Influence of temperature ramp-up and ramp-down with 20 °C interval on the catalytic activity of Mn(0.25)/TNT-H catalyst; gas hourly space velocity (GHSV) = 50,000 h^{-1}; feed: NO = 900 ppm, NO_2 = 100 ppm, NH_3 = 1000 ppm, O_2 = 10 vol.%, He carrier gas.

TiO_2 nanoparticles and also led to the formation of titania nanotubes (TNT-H) with the maximum specific surface area (SSA = 421 m^2/g) (Table 1). Conversely, alkaline hydrothermal treatment of TiO_2 (Sigma–Aldrich) led to the formation of lowest specific surface area (82 m^2/g) titania nanotube (TNT-SA). The specific surface area of the pristine titania nanotubes (TNT-H) dropped to 223 $m^2\,g^{-1}$ upon calcination. Interestingly, the Mn (0.25)/TNT-H sample calcined at 400 °C also showed 221 $m^2\,g^{-1}$ surface area (Table 2). These results indicate that the high dispersion of Mn species monolayer over the surface of titania nanotubes is achieved due to the involvement of Mn species with the titania nanotubes surface.

The adsorption/desorption isotherm types for as-synthesized titania nanotubes and manganese loaded nanotubes have also been investigated (Table 1) (Fig. S1 Supplementary material). As indicated in Table 1, most of the titania nanotube samples (TNT-H, TNT-I, TNT-SA, TNT-P25 and TNT-K) belong to V type of isotherms, while the isotherm of TNT-TOS sample belongs to IV type according to the IUPAC classification of adsorption/desorption isotherms. The IV isotherm reveals information on the mesopore structure and it is very close to the V type isotherm which shows weak absorbent–absorbate interaction [24]. The hysteresis loops exhibited by all the materials indicate that the resulting nanotubes are mainly mesoporous [14]. Most of the samples (TNT-I, TNT-SA, TNT-K, and TNT-P25), exhibit H1 type of hysteresis loop, which corresponds to uniform mesopores, while the type of hysteresis loop of N_2 isotherms in TNT-H and TNT-TOS samples is intermediate between H1 (at $0.5 < P/P_0 < 0.8$) and H3 (at $P/P_0 > 0.8$). H1 type that is a distinctive of uniform pores inside aggregates of particles has a tubular geometry and is open at both ends [14,25]. In conjunction with these results, the morphology of the synthesized titania nanotubes was also investigated by the high resolution transmission electron microscopy. The broad hysteresis loop of the samples such as TNT-H and TNT-I indicates a wide pore distribution confirmed by the pore size distribution data (Fig. S1) [25].

On the other hand, the type of the isotherms is identical before and after loading the manganese onto the surface of titania nanotubes signifying that the nanotube structure stays intact despite the calcination at 400 °C and the impregnation process. These results are in accordance with our HR-TEM results where the topographical morphology of the titania nanotubes did not change upon manganese loading and calcination. The selection of TiO_2 precursor has a strong influence on the pore size distribution patterns (Fig. S2). The TNT-H sample exhibits the largest pore volume in the range of 2–10 nm compared to the rest of the samples (Fig. S2). The samples TNT-I, TNT-K and TNT-P25 exhibit a small amount of pores in the macropore region (pore sizes larger than 50 nm).

3.4. X-ray diffraction

The X-ray powder diffraction patterns of different stages of the titania nanotubes prepared from TiO_2 (Hombikat) are shown in Fig. 6. For pure TiO_2 (Hombikat) sample, the strong characteristic peaks of titania typically at $d = 3.54$, 1.90, and 2.40 Å, which corresponds to anatase phase (JCPDS #71-1169) can be observed in our earlier studies [7,8]. To better understand the phase transformations, diffractograms of pure TiO_2 (P25 Degussa) is incorporated in Fig. 6. The P25 TiO_2 sample consists of 80% anatase and 20% rutile phase according to Eq. (1). The diffraction peaks corresponding to the anatase (PDF-#21-1272) phase (at $2\theta = 25.2°$, 37.9°, 48.1°, 54.0°, 55.1°, and 62.9°) and rutile (PDF-#21-1276) phase (at $2\theta = 27.4°$, 35.9°, and 41.2°) were observed for pure TiO_2 (P25 Degussa). As can be seen from the Figure, alkaline hydrothermal treated TiO_2 (Hombikat) showed the XRD peaks corresponding to the formation of sodium titanates ($Na_2Ti_3O_7$) phase (JCPDS #72-0148) [26,27]. Evolution of these peaks is subjected to the treatment of TiO_2 (Hombikat) with 10 M NaOH solution at 130 °C, where the shorter Ti–O bonds in TiO_6 units are expected to split and sodium ions are introduced into the structure. The resulting linear fragments would link to each other by $O^-{-}Na^+{-}O^-$ bonds to form flexible planar fragments. Further, washing of the sodium titanates with deionized water and HCl aqueous solution led to the evolution of diffraction peaks at $2\theta = 9.7°$, 24.7°, 28.6°, 48.4°, and 62.5° were observed, which can be attributed to (200), (110), (211), (020), and (422) planes of monoclinic $H_2Ti_3O_7$, respectively [19,25,28,29]. The replacement of Na^+ by H^+ would weaken the static interaction, resulting in the exfoliation of TiO_6 layers and subsequently leads to the formation of nanotubular structures. Moreover, the formation of a signature diffraction peak (200) at about $2\theta = 10°$ is the characteristic reflection attributed to $H_2Ti_3O_7$ phase in titania nanotube (Fig. 6b). Fig. 6 shows the powder XRD pattern of Mn/TNT-H calcined at 400 °C temperature for

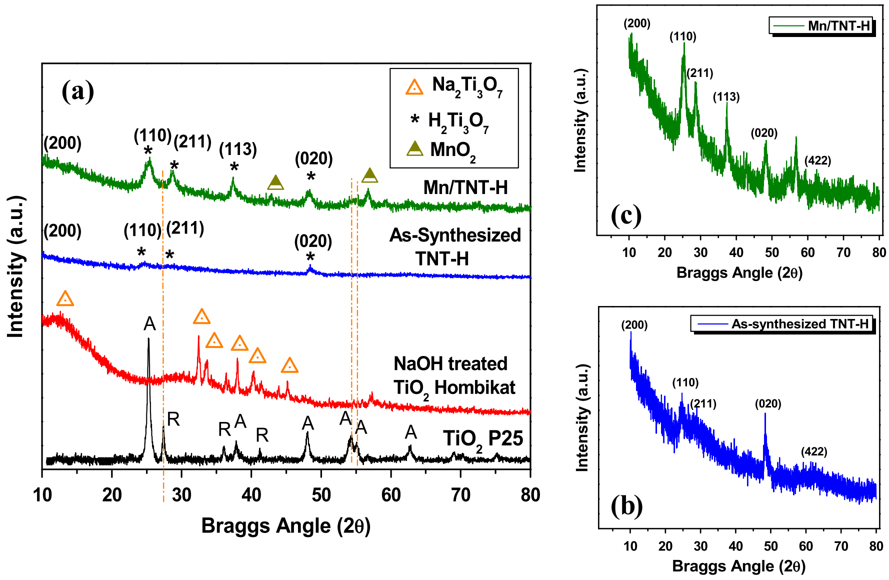

Fig. 6. Powder X-ray diffraction patterns of (a) TiO_2 P25, alkali treated TiO_2 Hombikat, as-synthesized TNT-H, Mn/TNT-H calcined at 400 °C for 2 h; (b) magnified X-ray diffraction profile of as-synthesized TNT-H and (c) magnified X-ray diffraction profile of Mn/TNT-H.

2 h. The characteristic XRD reflections shift to slightly larger angles at this temperature, indicating a decrease in the interlayer spacing in the titanate nanotube walls accompanied by removal of water. The intensity of the XRD peaks increased and new diffraction peak evolved at 37.3° which can ascribed to the (1 1 3) plane of $H_2Ti_3O_7$. In addition, the diffraction peaks at $2\theta = 42.7°$ and 58.0° correspond to the (1 1 1) and (2 1 1) planes of manganese dioxide (JCPDS card No. 24-0735) [8,9,30]. These results are in agreement with our TEM analysis where we can see a clear tubular structure of the catalyst.

$$\%X_R = 1 - \frac{1}{1 + \frac{1.26 \cdot I_R}{I_A}} \tag{1}$$

where I_R: XRD intensity of rutile (1 1 0) plane and I_A: XRD intensity of rutile (1 0 1) plane.

Effect of various TO_2 precursors on the synthesis of Mn/TNT nanotubes:

The powder X-ray diffraction patterns of various Mn/TNT-X samples calcined at 400 °C are shown in Fig. 7. Initially, titania nanotubes prepared by hydrothermal synthesis technique using various titania precursors namely, TiO_2 (Ishihara), TiO_2 (Kemira), TiO_2 P25 (Degussa), TiO_2 (Sigma–Aldrich), TiO_2 (Hombikat), TiO_2 are synthesized from titanium oxysulfate (TOS). Subsequently, manganese oxide confined titania nanotube catalysts were prepared by adopting the incipient wetness technique. These samples are denoted as Mn/TNT-I, MnTNT-K, Mn/TNT-P25, Mn/TNT-SA, Mn/TNT-H, and Mn/TNT-TOS, respectively, in Fig. 7. In addition, the diffractogram patterns of pure TiO_2 P25 are also presented for comparison. As one can see from the Fig. 7, all the Mn/TNT-X (X = I, K, P25, SA, H, and TOS) samples showed diffraction peaks at $2\theta = 9.7°$, 24.7°, 28.6°, 48.4°, and 62.5°, which can be ascribed to (2 0 0), (1 1 0), (2 1 1), (0 2 0), and (4 2 2) faces of monoclinic $H_2Ti_3O_7$, respectively. Among all the catalysts, only Mn/TNT-SA and Mn/TNT-K catalysts showed high intensity XRD peaks at $2\theta = 27.4°$, 36.1°, 41.4°, 54.2°, 56.7°, 62.8°, 64.0°, 69.1°, and 69.8° corresponding to (1 1 0), (1 0 1), (1 1 1), (2 1 1), (2 2 0), (0 0 2), (3 1 0), (3 0 1), and (1 1 2) planes of rutile TiO_2 phase in addition to the amorphous titania nanotubes ($H_2Ti_3O_7$ phase). These results illustrate the transformation of titania nanotubes to highly crystalline rutile TiO_2 in Mn/TNT-SA and Mn/TNT-K samples. This could be the reason for lower activity observed for Mn/TNT-SA and Mn/TNT-K catalysts compared to other formulations.

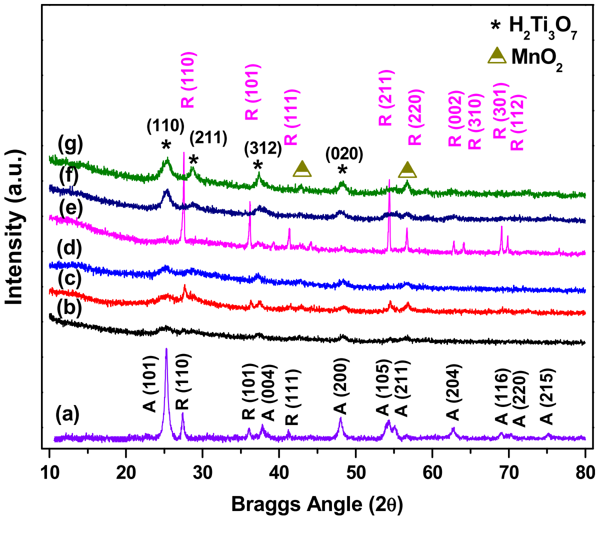

Fig. 7. Powder X-ray diffraction patterns of (a) TiO_2 P25, (b) Mn/TNT-I, (c) MnTNT-K, (d) Mn/TNT-P25, (e) Mn/TNT-SA, (f) Mn/TNT-TOS, and (g) Mn/TNT-H samples calcined at 400 °C for 4 h; A = anatase, and R = rutile.

3.5. Transmission electron microscopy

A series of titania nanotubes with two curled layers are successfully prepared by alkaline hydrothermal synthesis method and subsequent calcination. For an adequate determination of the morphology and textural properties of the pristine and manganese oxide confined titania nanotube (TNT-X and Mn(0.25)/TNT-X) samples were investigated by using high resolution transmission electron microscopy (HR-TEM/TEM) and illustrated in Fig. 8. As shown in Fig. 8, a large quantity of titania nanotubes with nearly uniform outer diameters approximately 9 nm can be observed, and a few isolated particles and plenty of intact nanotubes with inner diameter of approximately 3–6 nm, and length of several hundred nanometers ca. 100–300 nm were observed in the samples. The inner diameter of nanotubes fitted well with their pore size distribution curves (BET and Barrett–Joyner–Halenda) illustrated in Fig. S2. It can be clearly seen that all the spherical nanoparticles of titania transformed to nanotubes under the current experimental conditions, and all the nanotubes are open-ended with multi-wall as illustrated in Fig. 5. It has been well established in the literature and found in our current studies that the formation of tubular structure certainly depends on the titania phase composition [12,23,31]. Our HR-TEM studies illustrate that the well-defined tubular structures (Fig. 8a and b) are generated from rutile TiO_2 precursor (TiO_2 Sigma Aldrich, 95% rutile 5% anatase), whereas hierarchical two curled layers nanotubes formed with 100% anatase TiO_2 precursor (TiO_2 Hombikat) (Fig. 8c, d and h). The TiO_2 (Degussa, P-25) consisting of anatase and rutile crystalline phases (80% anatase, 20% rutile) also produced well-defined nanotubes (Fig. 8i). It can be observed from Fig. 8 that the rutile titania leads to the formation of uniform long length titania nanotubes (Fig. 8a and b) whereas the anatase phase leads to non-uniform fragmented nanotubes (Fig. 8c and d). Our high-resolution transmission electron microscopic (HR-TEM) investigations proved that the nanotubes still retain the tubular structure even after calcination at 400 °C. Moreover, Zhang et al. reported that the layered structure titanate phase can be preserved upon calcination at 400 °C, and the gradual interlayer dehydration leads to a crystal phase transformation of $H_2Ti_3O_7$ (protonated titanate) to anatase TiO_2 accompanied by the tubular structure into nanorods at above 500 °C [32].

The inset in Fig. 9a demonstrates the selected-area electron diffraction (SAED) pattern recorded on randomly oriented pristine titania nanotubes from TiO_2 Hombikat (TNT-H), and showed reflections characteristic of a tubular structure. Two spots at the edge of the zero spot were in proximity with the layered structure of nanotubes [33]. In particular, strong diffractions can hardly be identified, suggesting that the shells would consist of a quasi-two dimensional lattice [34]. Moreover, HR-TEM revealed that the nanotubes were multilayered and their interlayer spacing was observed at about 0.67 nm as illustrated in Fig. 9b which is in agreement with the previous reports [35]. The *d*-spacing of the lattice fringes was measured as 0.35 nm, which is in proximity to the (1 0 1) plane of anatase phase titania (Fig. 9a) [19]. Conversely, it is difficult to establish from TEM images whether the tiny manganese particles deposited inside the TiO_2 nanotube or outside the nanotubes, we could assume that the MnO_2 particles mainly exist inside the tubular channels of titania nanotubes [36]. Indeed, we could not find segregated manganese rich phases in our HR-TEM measurements for the studied materials. However, these techniques are limited to recognizing about the percent concentration minority phases [36]. Comparatively, X-ray Photoelectron Spectroscopy (XPS) is an adequate surface spectroscopic technique that

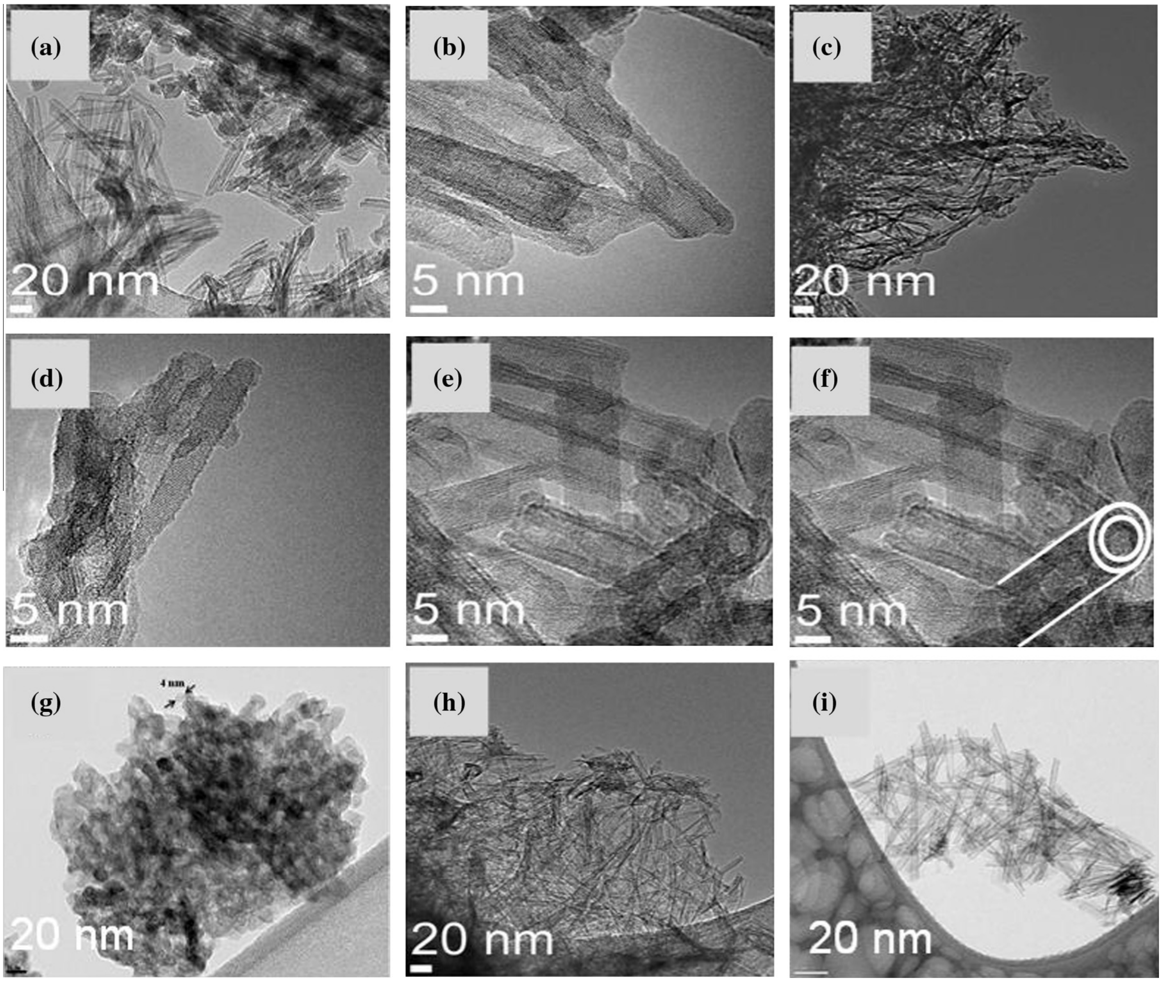

Fig. 8. Transmission electron microscopy images of pristine titania nanotube and manganese oxide confined titania nanotube formulations (a), (b) general and close view of Mn(0.25)/TNT-SA, (c and d) general view and tubular structure of Mn(0.25)/TNT-H, (e and f) evidence of foil structure and open ended nanotubes, (g) spherical nanoparticles of conventional TiO_2 Hombikat, (h) general view of TNT-H and (i) pristine TNT-P25.

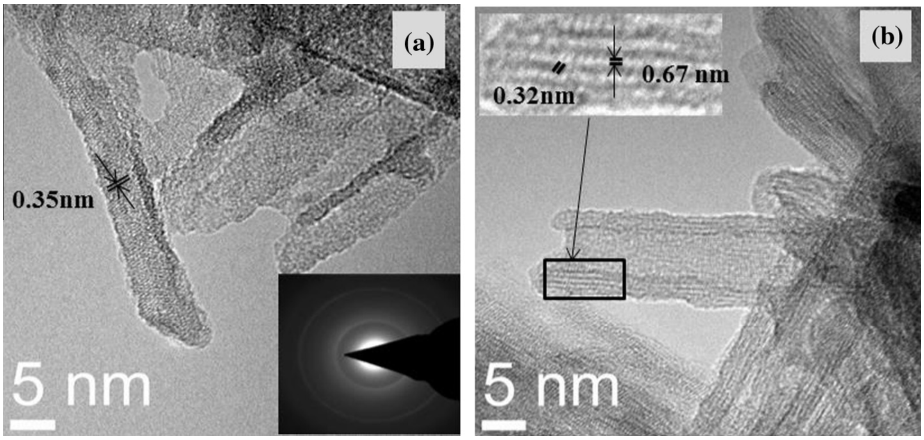

Fig. 9. (a) High resolution TEM image of the pristine titania nanotubes from TiO_2 Hombikat (TNT-H); inset is the selected-area electron diffraction (SAED) pattern, (b) HR-TEM images of Mn(0.25)/TNT-SA catalyst; inset is the enlarged picture of the tube wall confirming *d*-spacing of the lattice fringes 0.32 nm and the interlayer spacing 0.67 nm.

provides detailed specific oxidation state information of the microscopic local environment of the substituent metal cations in the catalyst in principle. As can be seen from Fig. 9b, the left inset is an enlarged picture of the tube wall (Mn(0.25)/TNT-SA). The periodicity of the fine fringes was 0.32 nm and the interspacing of the tube layers (walls) was 0.67 nm. We also observed a typical foil structure of titania nanotube in the HR-TEM image of Mn(0.25)/TNT-SA sample (Fig. 8f and e). The above results imply that the titania nanotubes were formed by rolling up the anatase single-layer sheets [11,37]. Our HR-TEM results are in good agreement with Raman spectroscopy analysis where the formation of Ti–O–Ti bonding and creation of oxygen vacancies have been established.

3.6. Raman spectroscopy

Raman scattering of pristine titania (Hombikat) (Fig. 10a), titania nanotubes (TNT-H) calcined at 400 °C (Fig. 10b) and the manganese oxide loaded titania nanotube (Mn(0.25)/TNT-H) (Fig. 10c) obtained in the present work are compared. For anatase TiO_2 (Hombikat), Raman scattering in manganese oxide loaded titania nanotube (Mn/TNT-H) exhibits vibrational modes that are weaker and broader in linewidth (compared to Fig. 10c to Fig. 10a). This result may be due to poor crystallinity of the Mn/TNT-H sample. To date, diverse structural models based on tetragonal anatase titania [34,35,38–45], monoclinic $H_2Ti_3O_7$ [46–49], monoclinic $H_2Ti_4O_9$ [50], orthorhombic $H_2Ti_2O_5{\cdot}H_2O$ [51,52] and orthorhombic $H_{0.7}Ti_{1.825}\square_{0.175}O_4{\cdot}H_2O$ (□: vacancy) [53,54] which consists of lepidocrocite (γ-FeOOH)-type TiO_6 octahedral host layers [55] have been proposed to understand the molecular structure of the titania nanotubes. Based on the these literature reports, the crystal structure of the titania nanotubes apparently depends on the synthesis conditions such as hydrothermal aging temperature, calcination temperature of the titania nanotubes and the concentration of NaOH, HCl and other alcohol solutions.

Anatase has tetragonal symmetry with two TiO_2 formula units (six atoms) per primitive cell. Anatase has the degree of symmetry, with point group 4/mmm in Hermann–Mauguin notation or D_{4h} Schönflies notation. Out of the 15 optical modes ($1A_{1g} + 1A_{2u} + 2B_{1g} + 1B_{2u} + 3E_g + 2E_u$) only the A_{1g}, B_{1g} along with E_g modes are Raman active while one A_{2u} mode as well as two E_u modes are infrared active whereas the B_{2u} mode is both Raman and infrared inactive [43,56,57]. In Fig. 10a, all the observed Raman active modes near 146 cm^{-1} (E_g), 396 cm^{-1} (B_{1g}), 517 cm^{-1} (A_{1g}), 640 cm^{-1} (E_g) can thus be identified with anatase-TiO_2. [39,58,59]. A mode near 442 cm^{-1} of E_g character and ascribed to the rutile-TiO_2 [59], is not observed in our Raman spectrum of either TNT-H or Mn/TNT-H nanotubes (Fig. 10b and c). These results are in agreement with our XRD analysis (Fig. 6). To better understand Raman scattering of our TNT-H calcined sample at 400 °C (Fig. 10b), the observed spectrum was deconvoluted as a superposition of Gaussians lineshapes. The selection of number and shape of the Gaussian peak was not arbitrary. Our best refinement of the features (Fig. 10b) observed near 396 cm^{-1}, 517 cm^{-1} and 640 cm^{-1} resulted when we deconvoluted these in terms of a broad band plus a narrow one with nearly the same centroid. The fraction of the majority to minority contribution to the lineshape features near 397 cm^{-1}, 518 cm^{-1}, and 639 cm^{-1} (Fig. 10b) was found to be about 94%:6%, and essentially provides a measure of the nanotube conversion from TiO_2 Hombikat nanoparticles. The majority of the scattering strength came from the broad bands with a minority of contribution coming from narrow ones. The broad band we ascribe to results from tubular nanotubes while the minority narrow peak from the promoter or precursor, viz., anatase TiO_2 Hombikat (Fig. 10a). It is interesting to note that using the hydrothermal synthesis technique and a heat treatment of the nanotubes at 400 °C, the promoter oxide does not apparently transform anatase phase to rutile. Furthermore, in the Raman spectrum of manganese oxide loaded titania nanotube (Mn(0.25)/TNT-H), the lowest frequency E_g phonon mode of anatase is blue-shifted from 146 cm^{-1} to 155 cm^{-1} (inset of Fig. 10c). The blue-shift of 9 cm^{-1} (Fig. 10c insert) is viewed to be due to the creation of oxygen vacancies [60]. These peak shifts are not due to the particle size effects. It has also been suggested that the four new modes observed near 126, 236, 256 and 301 cm^{-1} in the Raman spectrum of TNT-H sample can be ascribed to the formation of the tubular nanotube structure [59]. The reported values support well the modes observed in Fig. 10b for titania nanotubes synthesized in the present work using a hydrothermal technique. The deconvoluted Raman spectrum of Mn(0.25)/TNT-H shows modes near 123, 155, 207, 244, 303, 396, 518, 627, 711 and 814 cm^{-1}. The Raman modes in the 220–320 cm^{-1} range are ascribed to Ti–O vibrations; the lineshape resolution of these modes indicates a strengthening of Ti–OH bonds, which form an integral path of the tubular structure of the titania nanotubes [48,61]. The broad Raman bands near 244 cm^{-1}, 303 cm^{-1} and 396 cm^{-1} (Fig. 10c) could represent the second order scattering of the radial breathing oscillations (121 cm^{-1}, 151 cm^{-1} and 232 cm^{-1}) inherent to nanotubular structures [62]. In particular, the Raman peak mode near 300 cm^{-1} is due to the Ti–O bonds in titania nanotubes with layer structure (Fig. 10b and c) [63]. The overlapped new peak near 121 cm^{-1} could originate from left over Na–O bonds [64]. The red-shift by 13 cm^{-1} of the mode near 640 cm^{-1} (TiO_2-Hombikat) to 627 cm^{-1} in Mn/TNT-H (insert Fig. 10c) could indicate the formation of a new phase or possibly a new structural variant [59]. The 711 cm^{-1} peak can be attributed to the bending of the TiO_6 octahedral layers during the rolling process (Fig. 10c) [65]. The broad Raman bands around 800–950 cm^{-1} could be assigned to the stretching modes of short Ti–O bonds that stick out into the interlayer spaces of titania nanotubes [66,55,67].

On the other hand, low intensity broad bands of the second order of B_{1g} at 396 cm^{-1} phonon mode of anatase (Fig. 10a) and A_{1g} peak at 518 cm^{-1} were observed in pure TNT-H (Fig. 10b) and Mn(0.25)/TNT-H (Fig. 10c) samples. The broad nature of

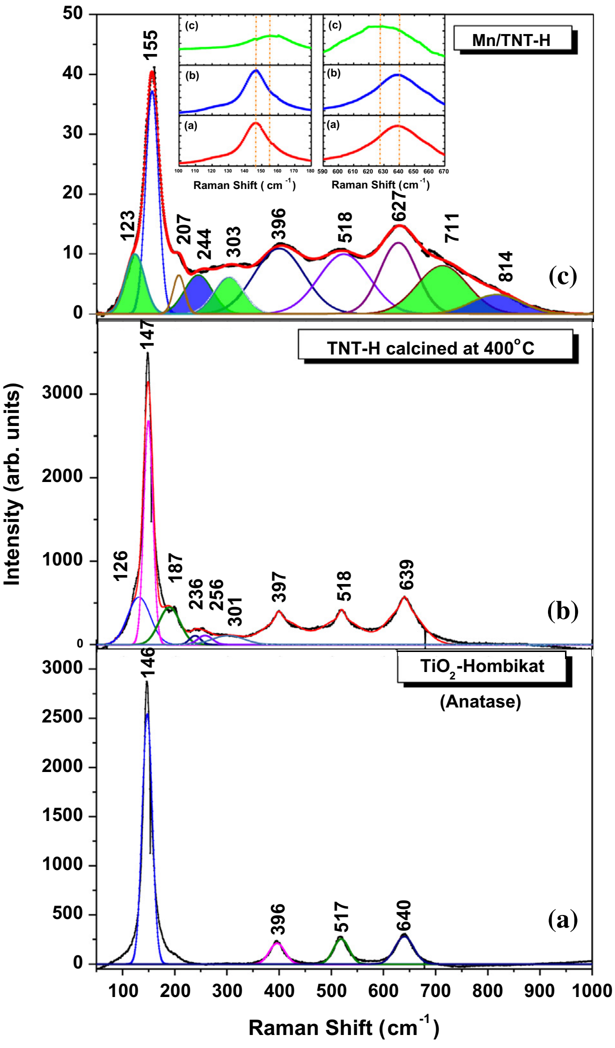

Fig. 10. The deconvoluted Raman spectra of (a) TiO_2 Hombikat (anatase), (b) TNT-H calcined at 400 °C (anatase) and (c) Mn(0.25)/TNT-H catalyst.

second order scattering modes is generally expected and may be promoted by crystalline disorder intrinsic to the nanotube structure in relation to TiO_2 nanoparticles. On the other hand, modes of MnO_2 at 650, 576 and 523 cm^{-1} and of Mn_2O_3 at 581, 509 and 630 cm^{-1} [68] were not observed in our Mn(0.25)/TNT-H sample as illustrated in Fig. 10c. The low scattering strength of Raman bands of Mn(0.25)/TNT-H sample compared to those of anatase-TiO_2 (Hombikat) and to pristine titania nanotubes (TNT-H) strongly suggests the role of structural disorder in promoting the observed behavior.

Our XRD results of various titania nanotubes confined manganese oxide catalysts do not show specific manganese crystalline phases and are thus in consistent with the Raman results. Rutile has tetragonal structure with two molecules in the unit cell with the space group D_{4h} ($P4_2$/mnm) and displays (Fig. 11a) four Raman active modes of B_{1g}, E_g, A_{1g} and B_{2g} symmetry near 144 cm^{-1} (B_{1g}), 442 cm^{-1} (E_g), 612 cm^{-1} (A_{1g}) and 826 cm^{-1} (B_{2g}) [69]. Raman scattering of TiO_2 SA nanoparticles (Fig. 11a) and TNT-SA nanotubes (Fig. 11b) shows modes characteristic of rutile-TiO_2 although they are broadened. These results illustrate that the B_{1g}, E_g and A_{1g} phonons and band near 239 cm^{-1} represent the characteristic features of rutile TiO_2 samples [70]. The B_{1g} mode is extremely sharp and B_{2g} mode at 826 cm^{-1} is virtually absent. These results also imply that there is little or no anatase to rutile phase transformation that underlies our synthesis of titania nanotubes. Although mode scattering strengths of rutile phase are quite low, the P25 TiO_2 nanoparticles sample demonstrates both Raman peaks corresponding to anatase and rutile (Fig. 11c). The TNT-P25 nanotubes sample exhibits modes only of the anatase phase (Fig. 11d). The TNT-H uncalcined nanotubes show similar Raman scattering profile as TNT-H calcined sample. However, low scattering strength and the broadening of the Raman bands could be observed for TNT-H uncalcined (Fig. 11e) compared to TNT-H calcined at 400 °C (Fig. 11b).

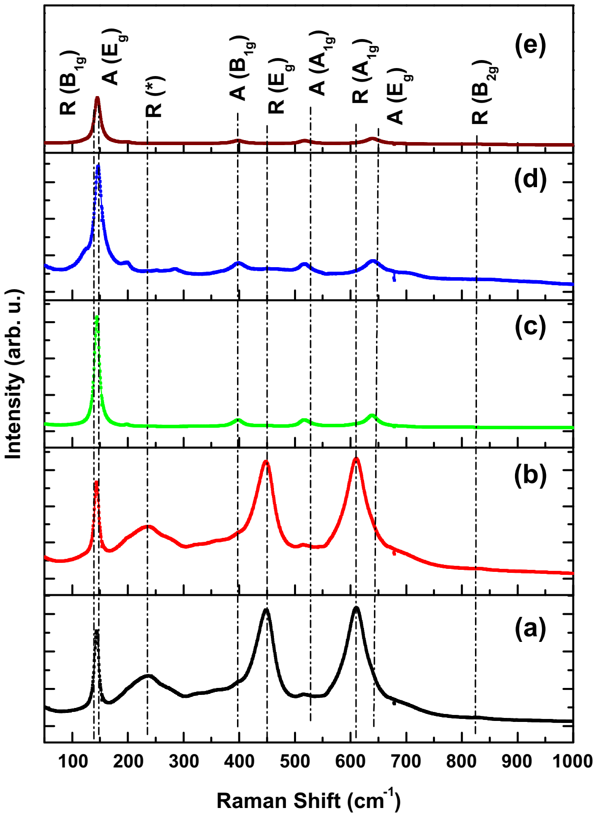

Fig. 11. The Raman spectra of (a) TiO_2 (Sigma–Aldrich) nanoparticles (rutile), (b) TNT-SA nanotubes (rutile), (c) TiO_2 (P25, Degussa) nanoparticles (anatase + rutile), (d) TNT-P25 nanotubes (anatase) and (e) TNT-H nanotubes uncalcined (anatase).

3.7. H_2-Temperature Programmed Reduction (H_2-TPR): Effect of titania nanotubes on reduction profile of Mn/TNTs

For an adequate determination of the effect of different titania nanotube supports on the reduction profile of manganese oxide, hydrogen-temperature programmed reduction (H_2-TPR) experiments were carried out. The reduction profiles for a series of manganese confined titania nanotubes synthesized from various titania precursors and Mn/Ti atomic ratio equal to 0.25 are illustrated in Fig. 12, while the reduction peak temperatures and the H_2 consumption in μmol g^{-1} are presented in Table 2. As it can be observed from Fig. 12, the manganese supported on conventional titania (Mn/TiO_2) catalyst shows three distinctive peaks corresponding to the stepwise reduction of MnO_2 to Mn_2O_3, Mn_2O_3 to Mn_3O_4 and Mn_3O_4 to MnO at 308, 404 and 482 °C, respectively. Conversely, the loading of manganese oxide into the titania nanotubes demonstrated only two reduction peaks. The low temperature reduction peak corresponds to the reduction of MnO_2 to Mn_2O_3 [7–9,71–74] and appears in the temperature range from 306 to 342 °C. The subsequent reduction temperature peak (306–342 °C) can be attributed to the reduction of Mn_2O_3 to Mn_3O_4 [7–9,71–74]. The high-temperature peak that is considerably smaller from the other two can only be observed in the spectra of Mn (0.25)/TNT-I, Mn(0.25)/TNT-P25, Mn(0.25)/TNT-K and Mn(0.25)/TiO_2 samples and appears at high temperatures from 386 to 430 °C corresponding to the reduction of Mn_3O_4 to MnO. Comparing the intensities of the peaks it can easily be concluded that the peak corresponding to the reduction of MnO_2 to Mn_2O_3 has higher intensity, indicating that Mn^{4+} oxidation state is dominant in the catalytic formulations compared to the Mn^{3+} and Mn^{2+} oxidation states which is confirmed by our XPS analysis.

As can be seen from Fig. 12, reduction peaks shifted to lower temperatures from top to bottom. Among all the catalysts prepared, Mn/TNT-H showed the highest shift of the manganese reduction temperature and could be an indication of positive

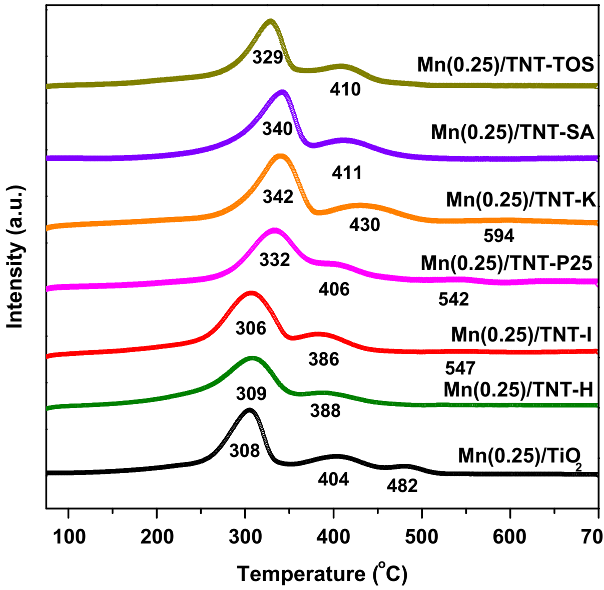

Fig. 12. Reduction profiles of manganese oxide confined titania nanotube formulations with Mn/Ti = 0.25 (Mn(0.25)/TNT-X), obtained from Hydrogen Temperature Programmed Reduction (H_2-TPR).

interaction between the titania nanotube support and the manganese oxide species. This interaction illustrates an enhancement of the oxygen mobility. It means the oxygen mobility was greatly enhanced due to the introduction of manganese oxide, which was beneficial to the SCR reaction. These results imply that the reduction potential of surface manganese species has been greatly increased by using Hombikat made titania nanotubes as supports [6].

In Fig. 13, Mn(x)/TNT-H (x = 0.15, 0.20, 0.25, 0.30, and 0.35) catalysts showed only two reduction peaks, varying the manganese oxide loading on the TNT-H support does not alter the reduction profile. As one can see from the figure, reduction peaks shifted to lower temperatures with increase in Mn/Ti atomic ratio up to 0.25. Further increase in manganese loading shifted the reduction peaks to higher temperatures. These results imply that the optimal manganese content reached with this atomic ratio in titania nanotubes. Both reduction peaks of Mn(0.25)/TNT-H sample have been shifted to much lower temperatures compared to the other samples indicating that the reduction potential of the surface Mn species is higher. The higher reducibility of surface active sites can be attributed to the better dispersion of manganese species on the support and also can be correlated with the highest deNO$_x$ potential of Mn(0.25)/TNT-H [7,8]. Earlier, SCR of NO over the pure manganese oxides at low-temperature was investigated by Kapteijn et al. [75] and found in our studies [8] that the NO conversions decreased in the order of $MnO_2 > Mn_5O_8 > Mn_2O_3 > Mn_3O_4$.

3.8. X-ray Photoelectron Spectroscopy (XPS)

To get insight about the oxidation state of manganese species and to ensure the chemical compositions (atomic concentrations) of the surface layer, we have investigated some selected potential catalysts by the X-ray Photoelectron Spectroscopy (XPS). The Mn (0.25)/TNT-SA, Mn(0.25)/TNT-K, Mn(0.25)/TNT-P25 and Mn (0.25)/TNT-H catalysts X-ray photoelectron spectra profiles have been shown in Fig. 14. The background was implemented in the routine and Gaussian functions have been used to describe the character of the peaks. The XPS spectra with fitted curves of the manganese-supported on different kind of titania nanotubes [rutile (K), rutile + anatase (SA), anatase + rutile (P25) and anatase (H)] calcined at 400 °C are shown in Fig. 14. In our earlier studies [7–9,74], XPS spectra of the reference samples of MnO_2, Mn_2O_3, Mn_3O_4, and MnO exhibited the Mn $2p_{3/2}$ peak at around 642.3, 641.3, 641.4, and 641.5 eV, respectively. Two main peaks due to Mn $2p_{3/2}$ and Mn $2p_{1/2}$ of the selected samples are shown in Fig. 14. For the identification of the surface manganese oxide phases and the relative percentages of Mn^{4+}, Mn^{3+}, Mn^{n+} species, the overlapped Mn 2p peaks were deconvoluted into several peaks by searching for the optimal combination of Gaussian bands with the correlation coefficients (r^2) above 0.99 (PeakFit, Version 4.0.6, AISN Software Inc.). The deconvoluted peaks are denoted as specific phases of manganese (MnO_2, Mn_2O_3, Mn-nitrate) in each spectrum (Fig. 14). The relative atomic concentrations of manganese and titania species were calculated by the area ratio of the corresponding characteristic peaks (Table 3). Table 3 shows the atomic concentrations of the catalysts determined by deconvoluted XPS spectra. The relative atomic percentage value of Mn^{4+}/Mn^{3+} characterized by deconvoluted XPS spectra was considerably high for the Mn(0.25)/TNT-H catalyst (Mn^{4+}/Mn^{3+} = 2.15) whereas, surface Mn^{3+} species are in equivalence with Mn^{4+} in other catalysts (Mn^{4+}/Mn^{3+} = 0.36–1.34) (Table 3, Fig. 14).

As can be seen from Fig. 11, MnO_2 and Mn_2O_3 coexisted over the surface of all the Mn-based catalysts. The surface Mn^{4+}/Mn^{3+} atomic ratio progressively enriched in the order of Mn(0.25)/TNT-SA $\ll$ Mn(0.25)/TNT-P25 < Mn(0.25)/TNT-K $\lll$ Mn(0.25)/TNT-H (Fig. 14 and Table 3), which may imply that the morphology of titania nanotubes and the phase of titania have very significant influence on concentration of the surface manganese species. On the other hand, the comparative manganese concentration over the titania nanotubes (Fig. 15) results suggested the elevated surface coverage of Mn species over the support, which can ascribed

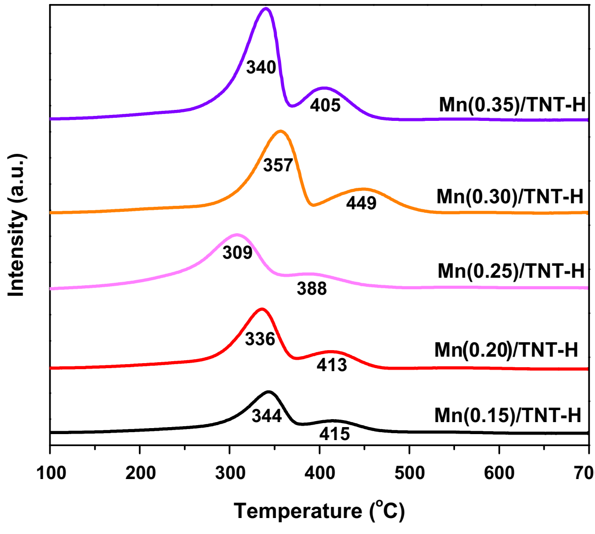

Fig. 13. Reduction profiles of manganese confined titanium nanotubes with different Mn/Ti ratio (Mn(x)/TNT-H) and on TiO_2 (Hombikat) with Mn/Ti = 0.25 (Mn(0.25)/TiO_2) obtained from Hydrogen-Temperature Programmed Reduction (H_2-TPR).

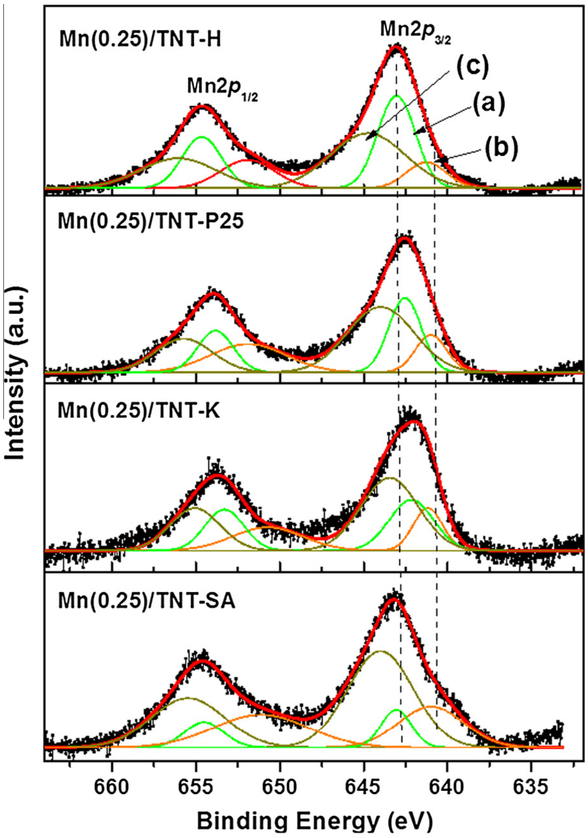

Fig. 14. Deconvoluted Mn 2p (XPS) spectra of Mn(0.25)/TNT-SA, Mn(0.25)/TNT-K, Mn(0.25)/TNT-P25 and Mn(0.25)/TNT-H catalysts: (a) MnO_2, (b) Mn_2O_3 and (c) Mn-nitrate.

Table 3
Binding energies and surface atomic ratios of active Mn species for the selected catalysts determined from deconvoluted XPS spectra.

Catalyst	B. E. (eV)					(Mn^{4+}/Mn^{3+})[b]	(Mn^{4+}/Mn^{n+})[b]	Mn/Ti[b]	Mn^{4+}/Ti[b]
	Ti $2p_{3/2}$	Ti $2p_{1/2}$	O 1s	Mn $2p_{3/2}$	Mn $2p_{1/2}$				
MnO_2[a]	–	–	–	642.1	653.6	–		–	–
Mn_2O_3[a]	–	–	–	641.3	653.0	–		–	–
Mn_3O_4[a]	–	–	–	641.4	652.9	–		–	–
MnO[a]	–	–	–	641.5	653.1	–		–	–
Mn(0.25)/TNT-SA	459.9	465.1	530.1	642.1 ± 0.2 641.3 ± 0.2	653.6 ± 0.2 653.0 ± 0.2	0.36	0.12	0.30	5.95E−02
Mn(0.25)/TNT-K	460.3	465.7	530.3	642.1 ± 0.2 641.3 ± 0.2	653.6 ± 0.2 653.0 ± 0.2	1.34	0.29	0.25	7.82E−02
Mn(0.25)/TNT-P25	460.5	465.9	530.1	642.1 ± 0.2 641.3 ± 0.2	653.6 ± 0.2 653.0 ± 0.2	1.18	0.29	0.36	1.10E−01
Mn(0.25)/TNT-H	459.4	464.8	530.8	642.1 ± 0.2 641.3 ± 0.2	653.6 ± 0.2 653.0 ± 0.2	2.15	0.38	0.67	2.25E−01

[a] Our earlier studies [8].
[b] Relative amounts are according to the metal atomic ratio determined from deconvoluted XPS spectra.

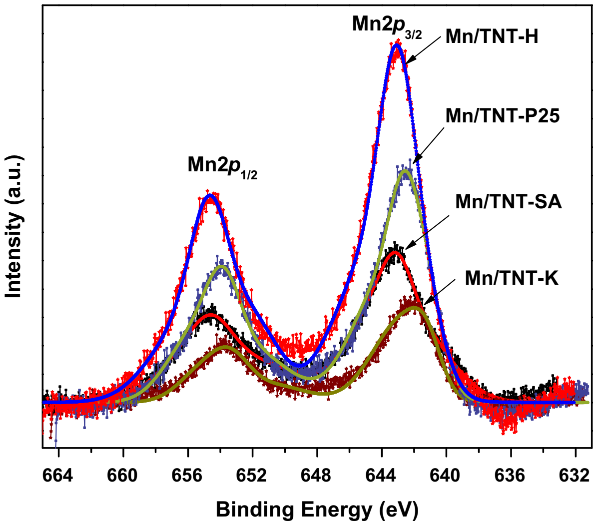

Fig. 15. Comparative Mn concentration over the surface of (a) Mn(0.25)/TNT-SA (Sigma Aldrich), (b) Mn(0.25)/TNT-K (Kemira), (c) Mn(0.25)/TNT-P25 (Degussa) and (d) Mn(0.25)/TNT-H (Hombikat) catalysts.

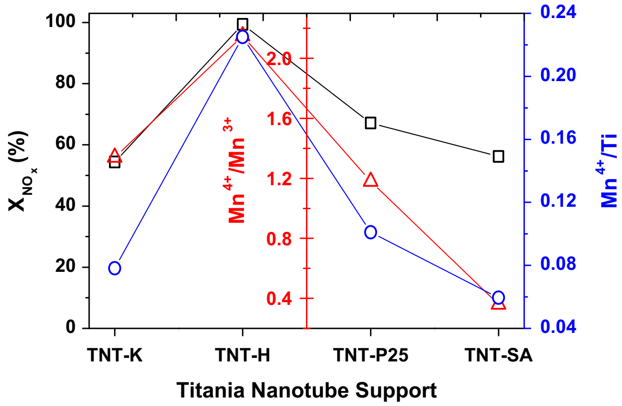

Fig. 16. Direct correlation of Mn^{4+}/Mn^{3+} and Mn^{4+}/Ti surface atomic ratios obtained from the deconvolution of XPS spectra with the catalytic activity of manganese oxide loaded titania nanotubes at 100 °C.

to the high dispersion of MnO_x species over the surface of TNT-H nanotubes.

Among the characterized catalytic formulations, Mn(0.25)/TNT-H exhibited high Mn^{4+} concentration ($Mn^{4+}/Ti = 0.22$), the rest of the catalytic formulations exhibit relatively lower Mn^{4+} surface concentration especially Mn(0.25)/TNT-SA sample exhibits very low value of Mn^{4+}/Ti (0.06). It is highly interesting to note that the relative atomic concentrations of Mn^{4+}/Mn^{3+} ratio and Mn^{4+}/Ti ratio are directly correlated with the potential SCR activity of the investigated catalysts (Fig. 16).

4. Conclusions

A series of manganese confined titania nanotube formulations with different morphological features were prepared by adopting alkaline hydrothermal synthesis technique and investigated for the selective catalytic reduction of NO_x by NH_3 at low-temperatures in the presence of excess oxygen. The resulting titania nanotubes possess different morphological features such as specific surface area, length and diameter due to the different characteristics of TiO_2 nanoparticles used for their synthesis. Among all the prepared samples, the Mn/TNT-H catalyst demonstrated remarkable $deNO_x$ performance and a wide temperature window in the temperature range of 100–300 °C. The selection of the TiO_2 precursor played a crucial role in the SCR activity of the Mn/TNT samples. The physicochemical characterizations were performed to better understand the structural morphology, catalyst engineering and potential $deNO_x$ performance in the low-temperature regimes. Our XRD results suggest only 6% of rutile to anatase phase transformation for the TNT-SA sample prepared from TiO_2 Sigma Aldrich (5% anatase, 95% rutile). The poresize distribution curves and H1 type of hysteresis loop imply a uniform mesopores inside the tubular geometry with open ends. Compared to manganese oxide supported on conventional TiO_2 UV-100 Hombikat, the synthesized catalysts exhibit superior activity in the whole temperature range. The activity of the manganese confined titania nanotube catalysts is attributed to the high surface area of the support, to the promotion of certain manganese oxidation states which are active for the low temperature SCR and the high amount of Lewis acid sites that have been reported to promote the low temperature activity. The Mn/Ti ratio of the catalytic formulations impacts the low temperature $deNO_x$ potential of the catalysts, when the ratio is low the acidity decreases and less active manganese sites are present to promote the reaction, increasing the manganese loading leads to active sites agglomeration thus impacting the activity of the catalyst. In particular Mn(0.25)/TNT-H sample demonstrated impressive NO_x conversions in the temperature range 100–300 °C in comparison with Mn/TiO_2 nanoparticles and other catalysts, which may be attributed to smaller particle size, scattered amorphous Mn over the catalyst surface, higher dispersion, and an abundant MnO_2 phase.

Appendix A. Supplementary material

Supplementary data associated with this article can be found, in the online version, at http://dx.doi.org/10.1016/j.jcat.2015.11.013.

References

[1] P.G. Smirniotis, D.A. Pena, B.S. Uphade, Angew. Chem. Int. Ed. 40 (2001) 13.
[2] M. Casanova, E. Rocchini, A. Trovarelli, K. Schermanz, I. Begsteiger, J. Alloys Compd. 408–412 (2006) 1108.
[3] T.J. Wang, S.W. Baek, H.J. Kwon, Y.J. Kim, I.-S. Nam, M.-S. Cha, G.K. Yeo, Ind. Eng. Chem. Res. 50 (2011) 2850.
[4] R.G. Gonzales, Diesel Exhaust Emission System Temperature Test, T&D report 0851-1816P, U.S. Department of Agriculture, 2008.
[5] D.S. Kim, C.S. Lee, Fuel 85 (2006) 695.
[6] K. Zhuang, J. Qiu, F. Tang, B. Xu, Y. Fan, Phys. Chem. Chem. Phys. 13 (2011) 4463.
[7] T. Boningari, P.G. Smirniotis, Appl. Catal. B Environ. 110 (2011) 195.
[8] T. Boningari, P.G. Smirniotis, J. Catal. 288 (2012) 74.
[9] D.A. Peña, B.S. Uphade, E.P. Reddy, P.G. Smirniotis, J. Phys. Chem. B 108 (2004) 9927.
[10] P.R. Ettireddy, N. Ettireddy, S. Mamedov, P. Boolchand, P.G. Smirniotis, Appl. Catal. B Environ. 76 (2007) 123.
[11] H. Ou, S. Lo, Sep. Purif. Technol. 58 (2007) 179.
[12] V. Idakiev, Z.-Y. Yuan, T. Tabakova, B.-L. Su, Appl. Catal. A Gen. 281 (2005) 149.
[13] S.-H. Chien, Y.-C. Liou, M.-C. Kuo, Synth. Met. 152 (2005) 333.
[14] C.-C. Tsai, H. Teng, Chem. Mater. 16 (2004) 4352.
[15] J.-N. Nian, S.-A. Chen, C.-C. Tsai, H. Teng, J. Phys. Chem. B 110 (2006) 25817.
[16] H. Wang, X. Chen, X. Weng, Y. Liu, S. Gao, Z. Wu, Catal. Commun. 12 (2011) 1042.
[17] X. Chen, S. Cao, X. Weng, H. Wang, Z. Wu, Catal. Commun. 26 (2012) 178.
[18] X. Chen, H. Wang, S. Gao, Z. Wu, J. Colloid Interface Sci. 377 (2012) 131.
[19] X. Chen, H. Wang, Z. Wu, Y. Liu, X. Weng, J. Phys. Chem. C 115 (2011) 17479.
[20] X. Chen, S. Gao, H. Wang, Y. Liu, Z. Wu, Catal. Commun. 14 (2011) 1.
[21] L. Xiong, Q. Zhong, Q. Chen, S. Zhang, Korean J. Chem. Eng. 30 (2013) 836.
[22] Q. Zhang, L. Gao, ÃJ. Sun, S. Zheng, Chem. Lett. 31 (2002) 226.
[23] D.L. Morgan, E.R. Waclawik, R. Frost, Adv. Mater. Res. 29–30 (2007) 211.
[24] K. Kaneko, J. Membr. Sci. 96 (1994) 59.
[25] D.V. Bavykin, V.N. Parmon, A. Lapkin, F.C. Walsh, J. Mater. Chem. 14 (2004) 3370.
[26] A. Thorne, A. Kruth, D. Tunstall, J.T.S. Irvine, W. Zhou, J. Phys. Chem. B 109 (2005) 5439.
[27] X. Cao, X. Xue, L. Zhu, P. Chen, Y. Song, M. Chen, J. Mater. Chem. 20 (2010) 2322.
[28] D.V. Bavykin, M. Carravetta, A.N. Kulak, F.C. Walsh, Chem. Mater. 22 (2010) 2458.
[29] E.M. Jr, P.M. Jardim, B.A. Marinkovic, F.C. Rizzo, M.A.S. de Abreu, J.L. Zotin, A.S. Araújo, Nanotechnology 18 (2007) 495710.
[30] C. Wei, H. Pang, B. Zhang, Q. Lu, S. Liang, F. Gao, Sci. Rep. 3 (2013) 2193.
[31] Y. Shiraishi, H. Hirakawa, Y. Togawa, Y. Sugano, S. Ichikawa, T. Hirai, ACS Catal. 3 (2013) 2318.
[32] L. Zhang, H. Lin, N. Wang, C. Lin, J. Li, J. Alloys Compd. 431 (2007) 230.
[33] C. Tsai, H. Teng, Chem. Mater. 18 (2006) 367.
[34] B.D. Yao, Y.F. Chan, X.F. Zhang, W.F. Zhang, Appl. Phys. Lett. 82 (2003) 281.
[35] T. Kasuga, M. Hiramatsu, A. Hoson, T. Sekino, K. Niihara, Adv. Mater. 11 (1999) 1307.
[36] P. Szirmai, E. Horváth, B. Náfrádi, Z. Micković, R. Smajda, D. Djokić, K. Schenk, L. Forró, A. Magrez, J. Phys. Chem. C 117 (2013) 697.
[37] S.S.S. Wong, Stony Brook, NY (US); Y. Mao, Los Angeles, CA (US), US Patents US 8,440,162 B1, May 14, 2013.
[38] T. Kasuga, M. Hiramatsu, A. Hoson, T. Sekino, K. Niihara, Langmuir 14 (1998) 3160.
[39] Y.Q. Wang, G.Q. Hu, X.F. Duan, H.L. Sun, Q.K. Xue, Chem. Phys. Lett. 365 (2002) 427.
[40] L. Qian, Z.-L. Du, S.-Y. Yang, Z.-S. Jin, J. Mol. Struct. 749 (2005) 103.
[41] G. Ali, H.J. Kim, J.J. Kim, S.O. Cho, Nanoscale 6 (2014) 3632.
[42] K.R. Moonoosawmy, M. Es-Souni, R. Minch, M. Dietze, M. Es-Souni, CrystEngComm 14 (2012) 474.
[43] F. Dong, H. Kelong, L. Shuqin, H. Jianhan, J. Braz. Chem. Soc. 19 (2008) 1059.
[44] Z. Zheng, B. Huang, J. Lu, Z. Wang, X. Qin, X. Zhang, Y. Dai, M.-H. Whangbo, Chem. Commun. 48 (2012) 5733.
[45] Y.G. Wang, X.G. Zhang, J. Electrochem. Soc. 152 (2005) A671.
[46] Y.G. Wang, X.G. Zhang, Electrochim. Acta 49 (2004) 1957.
[47] G.H. Du, Q. Chen, R.C. Che, Z.Y. Yuan, L.P. Peng, Appl. Phys. Lett. 79 (2001) 3702.
[48] Q. Chen, W. Zhou, G. Du, L.M. Peng, Adv. Mater. 14 (2002) 1208.
[49] Q. Chen, G.H. Du, A. Nakahira, W. Kato, M. Tamai, T. Isshiki, K.J. Nishio, Mater. Sci. 39 (2004) 4239.
[50] J. Yang, Z. Jin, X. Wang, W. Li, J. Zhang, S. Zhang, X. Guo, Z. Zhang, Dalton Trans. (2003) 3898.
[51] C.C. Tsai, H. Teng, Chem. Mater. 18 (2006) 367.
[52] J.N. Nian, H. Teng, J. Phys. Chem. B 110 (2006) 4193.
[53] R. Ma, Y. Bando, T. Sasaki, Chem. Phys. Lett. 380 (2003) 577.
[54] R. Ma, T. Sasaki, Y. Bando, Chem. Commun. (2005) 948.
[55] R. Ma, K. Fukuda, T. Sasaki, M. Osada, Y. Bando, J. Phys. Chem. B 109 (2005) 6210.
[56] K. Ozawa, Lithium Ion Rechargeable Batteries: Materials, Technology, and New Applications, Wiley, 2012.
[57] R.J. Gonzalez, R. Zallen, H. Berger, Phys. Rev. B 55 (1997) 7014.
[58] Y. Djaoued, S. Badilescu, P.V. Ashrit, D. Bersani, P.P. Lottici, J. Robichaud, J. Sol–Gel Sci. Technol. 24 (2001) 255.
[59] A. Orendorz, A. Brodyanski, J. Losch, L. Bai, Z. Chen, Y. Le, C. Ziegler, H. Gnaser, Surf. Sci. 601 (2007) 4390.
[60] J.C. Parker, R.W. Siegel, Appl. Phys. Lett. 57 (1990) 943.
[61] T.P. Feist, P.K. Davies, J. Solid State Chem. 101 (1992) 275–295.
[62] D.V. Bavykin, J.M. Friedrich, F.C. Walsh, Adv. Mater. 18 (2006) 2807.
[63] S.H. Byeon, S.O. Lee, H. Kim, J. Solid State Chem. 130 (1997) 110.
[64] F. Miyaji, T. Yoko, H. Kozuka, S. Sakka, J. Mater. Sci. 26 (1991) 248.
[65] T. Gao, H. Fjellvåg, P. Norby, Inorg. Chem. 48 (2009) 1423.
[66] S. Anderson, A.D. Wadsley, Nature (London) 187 (1960) 499.
[67] A. Kudo, T. Kondo, J. Mater. Chem. 7 (1997) 777–780.
[68] M.C. Bernard, A. Hugot Le Goff, B.V. Thi, S.C. De Torresi, J. Electrochem. Soc. 140 (1993) 3065.
[69] S.P.S. Porto, P.A. Fleury, T.C. Damen, Phys. Rev. 154 (1967) 522.
[70] C.A. Chen, Y.S. Huang, W.H. Chung, D.S. Tsai, K.K. Tiong, J. Mater. Sci.: Mater. Electron. 20 (2009) 303.
[71] H. Tong, Y. Huang, J. Air Waste Manage. Assoc. 62 (2012) 271.
[72] T. Boningari, P.G. Smirniotis, Catal. Lett. 141 (2011) 1399.
[73] T. Boningari, D.K. Pappas, P.R. Ettireddy, A. Kotrba, P.G. Smirniotis, Ind. Eng. Chem. Res. 54 (2015) 2261–2273.
[74] T. Boningari, P.R. Ettireddy, A. Somogyvari, Y. Liu, A. Vorontsov, C.A. McDonald, P.G. Smirniotis, J. Catal. 325 (2015) 145–155.
[75] F. Kapteijn, L. Singoredjo, A. Andreini, Appl. Catal. B 3 (1994) 173–189.